https://ntrs.nasa.gov/search.jsp?R=20160007649 2019-08-31T02:26:58+00:00Z

CFD Predictions for Transonic Performance of the ERA Hybrid Wing-Body Configuration

Karen A. Deere[1], James M. Luckring[2], S. Naomi McMillin[3], Jeffrey D. Flamm[4]
NASA Langley Research Center, Hampton, VA, 23681, USA

and

Dino Roman[5]
The Boeing Company, Huntington Beach, CA, 92647, USA

A computational study was performed for a Hybrid Wing Body configuration that was focused at transonic cruise performance conditions. In the absence of experimental data, two fully independent computational fluid dynamics analyses were conducted to add confidence to the estimated transonic performance predictions. The primary analysis was performed by Boeing with the structured overset-mesh code OVERFLOW. The secondary analysis was performed by NASA Langley Research Center with the unstructured-mesh code USM3D. Both analyses were performed at full-scale flight conditions and included three configurations customary to drag buildup and interference analysis: a powered complete configuration, the configuration with the nacelle/pylon removed, and the powered nacelle in isolation. The results in this paper are focused primarily on transonic performance up to cruise and through drag rise. Comparisons between the CFD results were very good despite some minor geometric differences in the two analyses.

Nomenclature

C_D	drag coefficient
C_L	lift coefficient
$C_{L,fixed}$	fixed lift coefficient for CFD solution
C_m	pitching moment coefficient
C_p	pressure coefficient
D	drag, lbf
F_1-F_4	four $C_{L,fixed}$ conditions (Table 1)
M	Mach number
M_1-M_{10}	ten Mach numbers (Table 1)
P_s	static pressure, psi
$P_{o,jet}$	jet total pressure, psi
T	thrust, lbf
$T_{o,jet}$	jet total temperature, °R
X or x	streamwise coordinate, in
Y or y	spanwise coordinate, in
Y1, Y2, Y3	three body locations for comparing C_p
Y4, Y5, Y6, Y7	four wing locations for comparing C_p
y^+	nondimensional first cell height
Z or z	vertical coordinate, in

Symbols

α	angle of attack, deg.

Acronyms

ARMD	Aeronautics Research Mission Directorate
CFD	Computational Fluid Dynamics
ERA	Environmentally Responsible Aviation
HWB	Hybrid Wing Body
IN	Isolated Nacelle
ISRP	Integrated Systems Research Program
PAI	Propulsion Airframe Integration
QCR	Quadratic Constitutive Relation
SA	Spalart-Allmaras (turbulence model)
UHB	Ultra-High Bypass ratio
WBT	Wing-Body-Tail
WBTNP	Wing-Body-Tail-Nacelle-Pylon

[1] Aerospace Engineer, Configuration Aerodynamics Branch, karen.a.deere@nasa.gov, AIAA Senior Member.
[2] Senior Research Engineer, Configuration Aerodynamics Branch, james.m.luckring@nasa.gov, AIAA Associate Fellow.
[3] Aerospace Engineer, Configuration Aerodynamics Branch, susan.n.mcmillin@nasa.gov.
[4] Aerospace Engineer, Configuration Aerodynamics Branch, jeffrey.d.flamm@nasa.gov, AIAA Associate Fellow.
[5] Associate Technical Fellow, Boeing Commercial Airplanes, dino.roman@boeing.com, AIAA Associate Fellow.

I. Introduction

The Environmentally Responsible Aviation (ERA) project within the Integrated Systems Research Program (ISRP) of the NASA Aeronautics Research Mission Directorate (ARMD) has the responsibility to explore and document the feasibility, benefits, and technical risk of air vehicle concepts and enabling technologies that will reduce the impact of aviation on the environment. The primary goal of the ERA project is to select air vehicle concepts and technologies that can simultaneously reduce fuel burn, noise, and emissions. Secondary goals include identifying and mitigating technical risk, as well as documenting new technologies and vehicle concepts for adoption into future aircraft designs.

One of the technology demonstrations within the Vehicle Systems Integration subproject is the Ultra-High Bypass Ratio (UHB) engine integration for Hybrid Wing Body (HWB) configurations. Figure 1 shows an artist's rendering of the HWB aircraft concept. The UHB engine integration for HWB technology demonstration seeks to quantify the impact of engine/airframe integration on HWB system performance and engine operability across key on- and off-design conditions. In concert with the goal to demonstrate an HWB Propulsion Airframe Integration (PAI) design concept that will enable fuel burn reductions in excess of 50% (1% drag penalty), is a metric to meet noise signatures leading to 42 EPNdB to Stage 4 noise margin for the aircraft system.

Figure 1. An artist's rendering of an HWB aircraft concept.

NASA partnered with Boeing to design and verify an HWB PAI concept that minimizes adverse propulsion/airframe shielding to meet ERA noise reduction metrics. The project must demonstrate reduced component induced interference effects that could result in high drag or poor aerodynamic characteristics[1]. NASA and Boeing used computational fluid dynamics (CFD) predictions and a series of wind tunnel tests to quantify key design trade-space issues that impact UHB engine operability in HWB concepts and to minimize the impact of adverse effects on the aerodynamic metrics. A 5.75% scale model of the HWB concept was tested in the NASA Langley Research Center (LaRC) 14x22 Low Speed Wind Tunnel and the National Full-Scale Aerodynamics Complex (NFAC) 40x80 Low Speed Wind Tunnel, located at the NASA Ames Research Center, to characterize the impact of airframe dominated flows on the fan stall margin of a UHB concept and to characterize the impact of propulsion induced flows on the performance and stability and control of an HWB configuration.

Characterizing the performance of new aircraft designs, such as the HWB configuration, is a complex process. Computational tools typically play an important role to supplement experimental data. However, several project constraints resulted in the elimination of the high-speed, transonic experimental testing portion of the ERA project. Thus, characterizing high-speed, transonic performance became solely the responsibility of CFD. Therefore, two completely independent numerical assessments were performed to add confidence to the CFD predictions. This

paper highlights a portion of the CFD that was completed to understand the high-speed, transonic performance of the HWB. The current results were also used in an independent assessment of the process of determining interference drag, which was one high-level performance metric used to quantify the success of the HWB configuration in the NASA ERA project.

The Boeing Company used a proprietary process for determining the interference drag of the HWB configuration that was reported to the ERA project. Although this provided a very realistic assessment for the drag increment, it also meant that NASA could not replicate the process to produce this increment. However, NASA conducted an independent CFD analysis for the primary CFD results that provided the input to the interference drag assessment. Coupled with a review of the Boeing approach to the interference drag assessment, this then led to the independent assessment by NASA of the project performance metric on interference drag. This paper describes the independent CFD assessments that were performed.

Three related configurations were analyzed. The first configuration was the full wing-body-tail with the powered nacelle and pylon (WBTNP) at cruise conditions (thrust = drag). Center elevon deflection effects related to trim were also assessed for this configuration. The second configuration had the nacelle/pylon removed (wing-body-tail, WBT). The third configuration was the powered nacelle in isolation. Primary CFD analyses of these configurations were performed by Boeing using the overset structured-grid code OVERFLOW as part of their interference drag assessment process. Secondary analyses were performed by NASA LaRC using the unstructured-grid code USM3D. Both analyses followed their own independent standard practices. All computations were performed with full-scale geometry at full-scale flight conditions.

The analysis presented in this report is focused on drag up to and through drag rise (fixed lift coefficient). Some pressure distributions are also included. Due to the sensitive nature of the work, numerical values for the flow conditions as well as the outcome coefficients were omitted. Quantitative increments, however, are included in the figures. The CFD results were obtained for ten Mach numbers (referred to hereafter as M_1 through M_{10}) and four fixed lift coefficients (referred to hereafter as F_1 through F_4). The cruise condition for the HWB corresponded to the Mach number M_8 and the lift coefficient F_3. The configurations analyzed are discussed in the next section, followed by a summary of the CFD methods used, the flow conditions for the study, and the results. Concluding remarks are also provided.

II. Configurations

Three configurations were selected for this study that follow fairly standard transonic performance analysis, including component buildup effects and interference assessments. The first configuration was the full wing-body-tail with the powered nacelle and pylon. The second configuration had the nacelle/pylon removed (wing-body-tail). The third configuration was the powered nacelle in isolation. All configurations were modeled at full scale.

The outer mold line for the HWB evolved during the execution of the ERA project, and one consequence was that the configurations used for the Boeing analyses were slightly different from those used for the NASA analyses. However, the configuration differences were small enough to warrant the comparison study reported herein.

A. HWB Wing-Body-Tail-Nacelle-Pylon Configuration

The full-scale, HWB WBTNP configuration included the hybrid wing body with tails, nacelles and pylons. For this configuration, very small differences are expected between OVERFLOW and USM3D results due to a small geometry difference on the pylon trailing edge. The LaRC team began with a configuration that had a longer pylon geometry with a single trailing-edge sweep angle. As the design matured, Boeing investigated a shorter pylon with a compound trailing-edge sweep angle. A structured-grid representation of the right semispan of this configuration is shown in Figure 2.

All of the computations for this configuration were performed with a powered nacelle. Trim was also addressed by Boeing through computations with a variety of control surface deflections. The majority of the CFD performed by NASA was for the baseline configuration with no control surface deflections. However, limited CFD was performed by NASA for a center elevon deflection of +3° and -3° to support code-to-code assessments of control surface effects used to achieve trim.

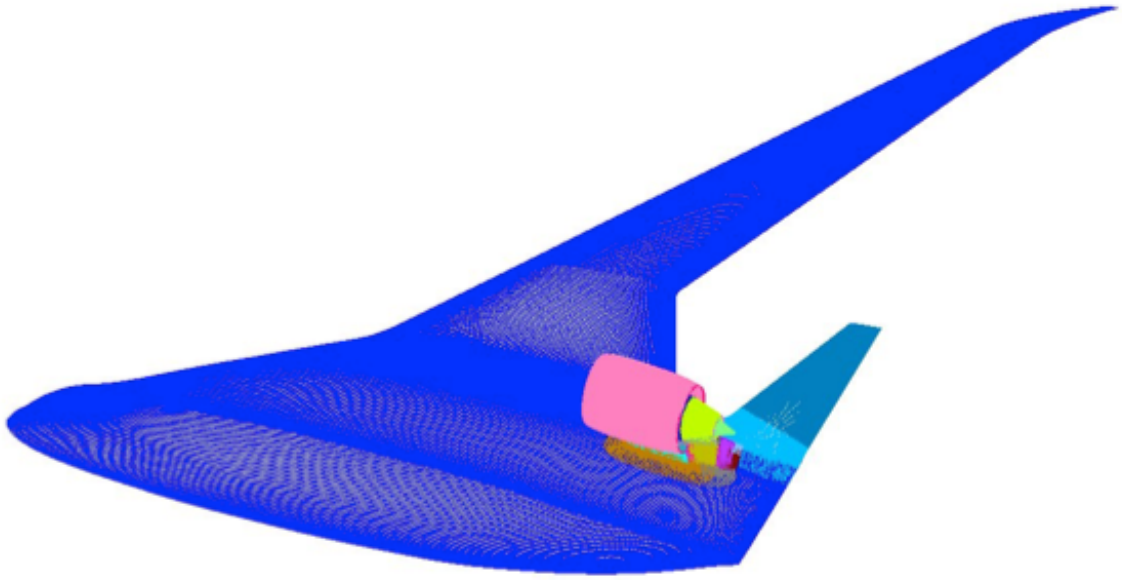

Figure 2. An OVERFLOW 30-block overset surface grid for the right semispan HWB WBTNP configuration.

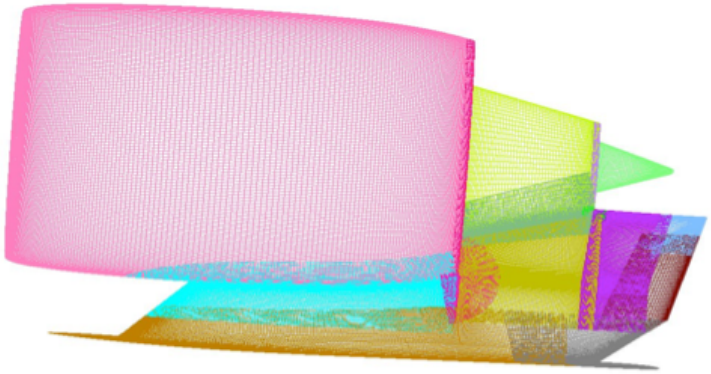

(a) OVERFLOW surface mesh of the nacelle/pylon components.

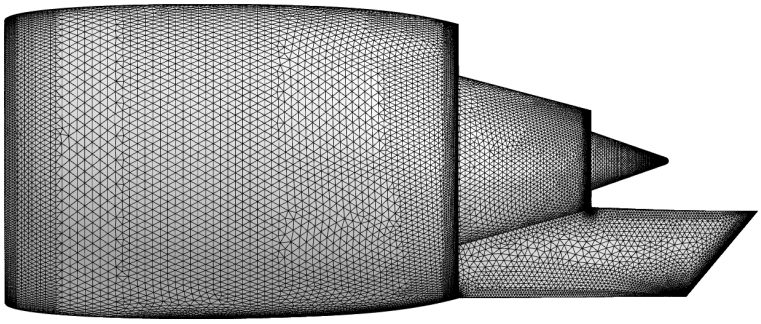

(b) USM3D unstructured surface grid for the isolated nacelle.

Figure 3. Surface mesh details of the nacelle components of the WBTNP configuration.

B. HWB Wing-Body-Tail Configuration

This configuration had the nacelle/pylon removed from the full configuration just described. The geometry used in the NASA/USM3D computations was created by simply removing the nacelles and pylons from the WBTNP geometry. However, the geometry used in the Boeing/OVERFLOW computations was an aerodynamically improved HWB WBT geometry, with slight differences, that was used in the calculation of interference drag. Therefore, small differences were once again expected between the OVERFLOW and USM3D results due to geometry differences. Despite this small geometry difference, the baseline wing-body-tail configuration was viewed as a valuable baseline for comparing the computational results due to the absence of the nacelle/pylon geometry along with power-induced effects. The WBT configuration is one of the key components in computing interference drag.

C. Isolated Nacelle

The third configuration was the isolated nacelle (IN) geometry that included the bifurcator and shelf. This geometry was slightly different between the Boeing/OVERFLOW and NASA/USM3D computations. Figure 3(a) shows the nacelle and pylon detail for the OVERFLOW solutions, but the pylon was removed for the isolated nacelle analysis. Figure 3(b) shows the isolated nacelle surface mesh used for the USM3D solutions. The geometry for the USM3D solutions had a longer bifurcator shelf and therefore, the closeout angle was also different between the two geometries. All computations for this configuration were powered. The isolated powered nacelle is another of the key components in computing interference drag.

III. OVERFLOW Method and HWB Modeling

The OVERFLOW code[2] is a node-based Reynolds Averaged Navier-Stokes (RANS) code specifically designed for structured overset grid systems. This NASA-developed and -maintained program is updated on a regular basis with contributions from government, academia and industry. It is considered to be a general-purpose 2D/3D solver capable of simulating steady and unsteady flows over a wide range of Mach numbers using a number of different approaches. Depending on the type of simulation, the solver can be run in 2D or 3D, thin-layer or full Navier-Stokes, central or upwind differencing, static or moving body.

All OVERFLOW computations were performed by Boeing. The computations were performed with their own proprietary version of the code, and this code was the primary tool for determining transonic aerodynamic performance and interference drag increments. OVERFLOW standard practices developed at Boeing were followed in all aspects of the computational study.

A. Grid Generation

The lofted outer mold line definition was exported from the CATIA solid model to an IGES file. The structured surface gridding was done in MADCAP, a grid-generation package developed at Boeing that is capable of unstructured and structured grid generation.[3] The overset volume grids were built using HYPGEN, LEGRID, SMOGRD and BOXGR software.[4,5] Grid connectivity was achieved with PEGASUS5 software.[6] Finally, an integration surface was generated using MIXSUR. Best practice gridding guidelines were followed as discussed in Reference 7. A 30 block, 58.5 million point overset volume grid was generated for the right semispan of the HWB WBTNP configuration as shown in Figure 2. The grids were made with a y^+ value of approximately 1 for the cruise condition. The far field boundary was located 22 body lengths from the configuration.

B. Computational Flow Solver and Solution Procedure

The full Navier-Stokes equations were solved using a 3rd-order Roe upwind differencing scheme. Turbulence was represented by the Spalart-Allmaras turbulence model with the Quadratic Constitutive Relation (QCR).

No-slip boundary conditions were used on all solid surfaces. Engine power was simulated by specifying P_s to match the massflow at the fan face, and $P_{o,jet}$ and $T_{o,jet}$ were set at the fan and core exit planes for the particular flight condition of interest.

The force and moment calculations were accomplished using the FOMOCO computer code as described in reference 8.

C. Convergence Criteria

Solutions that started from scratch were run to 13000 cycles and solutions that were restarts from another condition were run an additional 7000 cycles. Solutions included three levels of multigrid to ensure convergence. A figure of merit was drag converged to within 0.1 count within the last 1000 cycles of the solution.

IV. USM3D Method and HWB Modeling

The NASA Tetrahedral Unstructured Software System (TetrUSS) was used for this computational analysis.[9] TetrUSS includes a model preparation tool (GridTool), grid generation software (VGRID, POSTGRID) and a computational flow solver (USM3D). The TetrUSS flow solver USM3D is a tetrahedral cell-centered, finite volume RANS method. The USM3D code has a variety of options for solving the flow equations and several turbulence models for closure of the RANS equations.[9,14] The USM3D flow solver has internal software to calculate forces and moments. Additionally, the NASA LaRC-developed code USMC6 was used for analyzing the solutions.[10]

All USM3D computations were performed by NASA LaRC. These computations were performed to provide an independent assessment of the transonic aerodynamic performance including the constituent components that go into an interference drag increment analysis. USM3D standard practices developed at NASA were followed in all aspects of the computational study.

A. Grid Generation

The lofted outer mold line definition was exported from the CATIA solid model to an IGES file for input to GridTool[11] for geometry preparation. Surface patches were created on the configuration and sources were placed throughout the domain to accurately capture configuration characteristics. The output from GridTool was used to automatically generate the computational domain with the VGRID unstructured grid generation software. The VGRID software used an Advancing Layers Method to generate thin layers of unstructured tetrahedral cells in the viscous boundary layer, and an Advancing Front Method to populate the volume mesh in an orderly fashion.[12,13] Finally, POSTGRID was used to close the grid by filling in any gaps that remain from VGRID. POSTGRID is automated to carefully remove a few cells surrounding any gaps in the grid and precisely fill the cavity with the required tetrahedral cells without gaps to finalize the mesh.

The geometry and computational domain were specified in full-scale inches. The computational domain extended approximately 20 body lengths from the configuration in the x, y and z directions. The unstructured mesh contained 50 million cells for the HWB WBTNP and 25 million cells for the HWB WBT configurations. The mesh of the isolated nacelle contained 22 million cells. The first cell height in the boundary layer mesh was specified for y^+ values less than one.

B. Computational Flow Solver and Solution Procedure

This study used the implicit Gauss-Seidel scheme and the Roe flux difference-splitting scheme. The code was run in first order spatial accuracy until the residual dropped two orders of magnitude. Then, the code automatically switched to generate second order spatially accurate solutions. The SA turbulence model was used for all of the flow conditions. The SA turbulence model was implemented with a first order advection term. The QCR option was not available in USM3D.

No-slip boundary conditions were used on all solid surfaces. A subsonic inflow boundary condition was used at the inflow face of the domain and an extrapolation boundary condition was used at the downstream outflow face of the domain. A characteristic inflow and outflow boundary condition was used along the far field, lateral faces of the domain. Powered simulations were computed using the turbofan engine boundary condition. The fan and core jet boundary conditions were set with values for $P_{o,jet}$ and $T_{o,jet}$. Flow at the inlet-plane was determined automatically through a mass flux balance with the core and fan flow.

For each iteration, the USM3D code computed the forces and moments for the total configuration and for each component. The values were used to track the convergence throughout the solution development. The Langley-developed post-processing tool, USMC6, was also used to extract data for post-processing and plotting data.

C. Convergence Criteria

Two main criteria were used to monitor and determine USM3D solution convergence. First, a drop in residual (L2-norm of the mean flow residue) of at least three orders of magnitude was required. Second, the convergence of C_L, C_D and C_m was considered achieved when the maximum variation of the coefficient over 2000 iterations was less than 0.1% of the average coefficient value computed over the same range of iterations.

V. Flow Conditions

Solutions were computed over a range of Mach numbers from moderate subsonic through transonic conditions that included drag rise. The various Mach numbers investigated were labeled, in increasing values from subsonic to transonic values, M_1 to M_{10} for discussion purposes. Likewise, the four fixed lift coefficient ($C_{L,fixed}$) conditions that were investigated are labeled in increasing values: F_1, F_2, F_3, and F_4. The cruise design condition was at $M = M_8$ and $C_{L,fixed} = F_3$. The fixed-lift-coefficient solutions were achieved through iterative angle-of-attack adjustments. All solutions were computed at full-scale flight Reynolds numbers. All powered CFD cases were run with conditions for thrust equal to drag (T=D).

A summary of the matrix of computed flow conditions and configurations is shown in Table 1. Powered CFD results were obtained for the HWB WBTNP configuration across the full range of Mach numbers (subsonic through transonic) for the fixed lift coefficient F_3 with the exception of M_2. Powered results were also obtained at one transonic Mach number (M_8) for the four fixed lift coefficients. The unpowered CFD results were also obtained for the HWB WBT configuration across the full range of Mach numbers, but for three fixed lift coefficients (F_2, F_3, and F_4). Finally, powered CFD data for the isolated nacelle geometry were compared at the cruise design point (M_8, F_3).

Table 1. Matrix of flow conditions.

Mach	$C_{L,fixed} = F_1$	$C_{L,fixed} = F_2$	$C_{L,fixed} = F_3$ *(cruise)*	$C_{L,fixed} = F_4$
M_1		WBT	WBT, WBTNP	WBT
M_2		WBT	WBT	WBT
M_3		WBT	WBT, WBTNP	WBT
M_4		WBT	WBT, WBTNP	WBT
M_5		WBT	WBT, WBTNP	WBT
M_6		WBT	WBT, WBTNP	WBT
M_7		WBT	WBT, WBTNP	WBT
M_8 *(cruise)*	WBTNP	WBT, WBTNP	WBT, WBTNP, IN	WBT, WBTNP
M_9		WBT	WBT, WBTNP	WBT
M_{10}		WBT	WBT, WBTNP	WBT

VI. Results

A baseline solution for the full powered configuration (WBTNP) at cruise conditions is shown in Figure 4 from the OVERFLOW analysis. Transonic shocks can be observed on the wings and the nacelles, and the powered HWB sustains attached flow over the full configuration with the exception of the aft pylon/body juncture and a small conical zone aft of the pylons on the body.

Analysis for the drag characteristics of the hybrid wing-body will first be presented for the unpowered WBT configuration (nacelles and pylon removed). Next the powered WBTNP configuration will be presented, followed by results for the isolated powered nacelle. Most results presented will be drag rise curves (fixed lift coefficient). Some selected pressure coefficient (C_p) distributions are also included.

A. Unpowered HWB Performance

Analysis is first presented for the performance of the HWB WBT at the design lift condition. Figure 5 shows the comparison of results for drag coefficient (C_D), lift coefficient (C_L), and angle of attack (α), between OVERFLOW and USM3D, for the HWB WBT configuration over $M_1 < M < M_{10}$ at the design lift coefficient ($C_{L,fixed} = F_3$). The results between the codes agree very well, with drag coefficient within 1 count of drag and the angle of attack within 0.05 degrees at each Mach number. The lift coefficient plot shows how tightly the fixed lift condition was achieved, and the variation in the USM3D results was due to the particular tolerance used for these results. The effect of tightening this tolerance will be addressed later in this section.

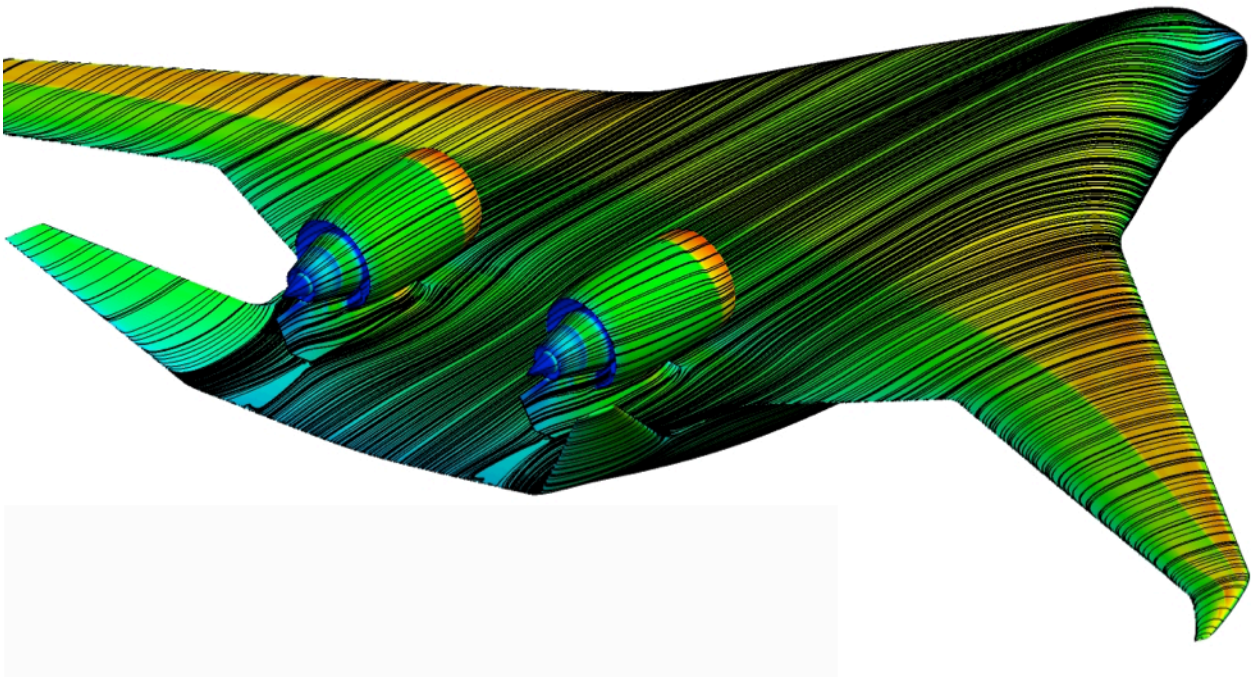

Figure 4. A Boeing OVERFLOW solution on the HWB WBTNP configuration at cruise.

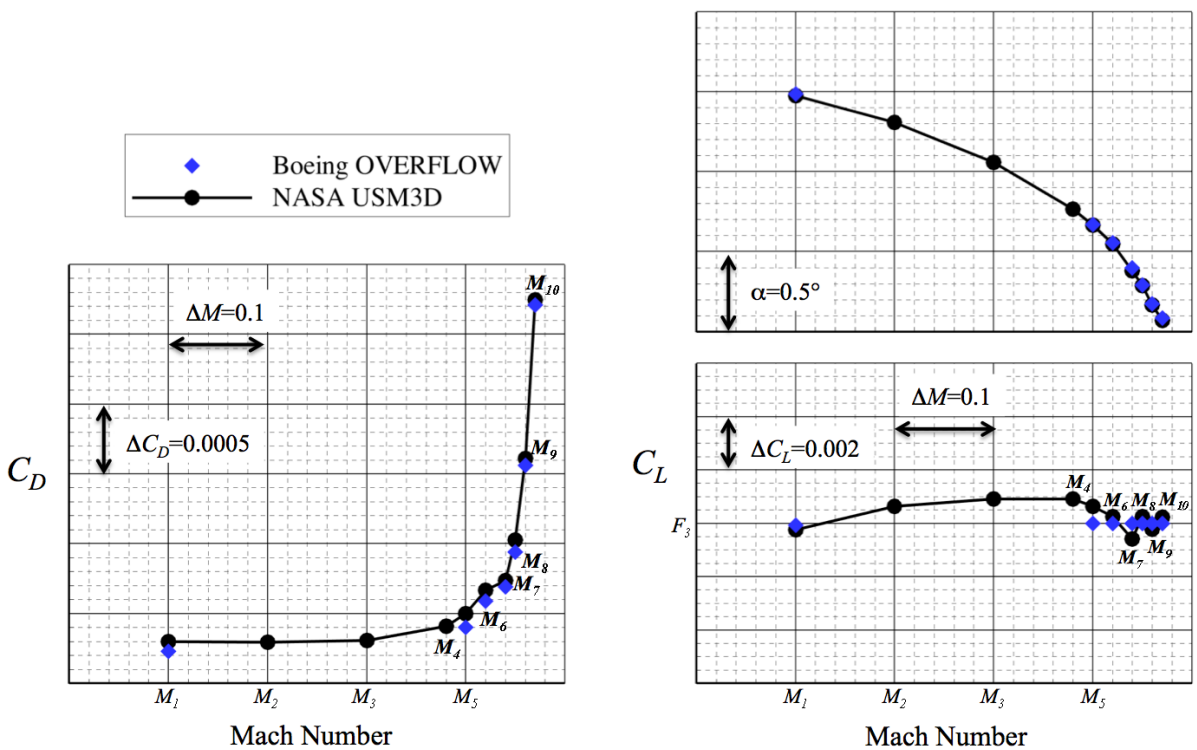

Figure 5. Comparison of C_D, C_L, and α between the two codes for the HWB WBT configuration for $M_1 \leq M \leq M_{10}$ at $C_{L,fixed} = F_3$.

This close agreement between the codes is also evident in Figure 6, which shows the drag coefficient results from the USM3D and OVERFLOW computations at the cruise Mach number ($M = M_8$) and three fixed lift coefficients ($C_{L,fixed} = F_2, F_3$, and F_4). The difference in drag coefficient between the two codes ($C_{D,OVERFLOW} - C_{D,USM3D}$) is within 1.1 counts of drag for all three fixed lift coefficient conditions. Figure 7 shows the pitching moment coefficient (C_m) results for the same conditions with a slightly larger difference between the codes for C_m data at F_2 and F_3 than at F_4. The difference in pitching moment coefficient between the two codes ($C_{m,OVERFLOW} - C_{m,USM3D}$) is within 0.0002 to 0.0005 for all three fixed lift coefficients. The corresponding center of pressure differences between the two predictions were within 0.06 to 0.23 percent reference chord. A couple of possible explanations for the pitching moment differences between OVERFLOW and USM3D are a potential difference in shock location on the wing body or a difference in the afterbody geometry having a larger effect at F_2 and F_3.

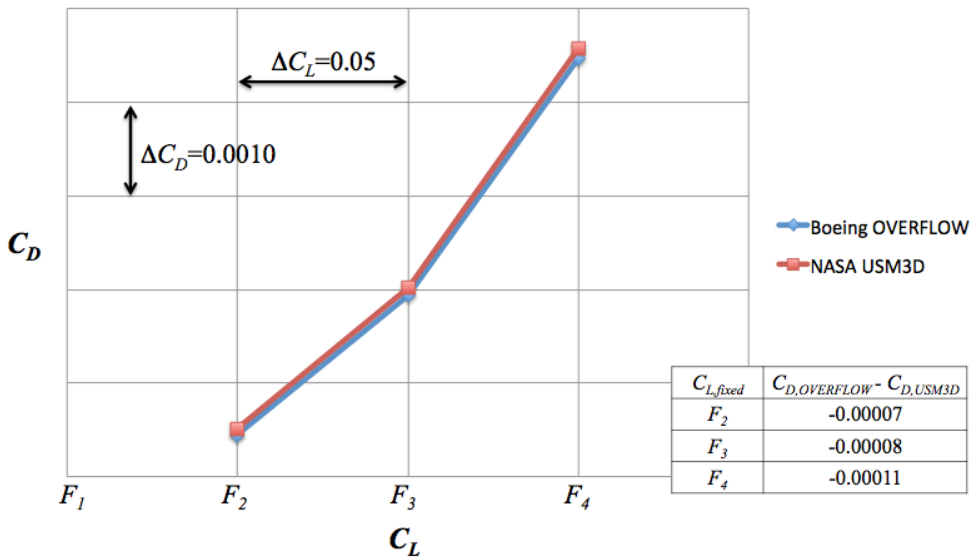

$C_{L,fixed}$	$C_{D,OVERFLOW} - C_{D,USM3D}$
F_2	-0.00007
F_3	-0.00008
F_4	-0.00011

Figure 6. Comparison of C_D between the two codes for the HWB WBT configuration for $M = M_8$ at $C_{L,fixed} = F_2$, F_3, and F_4.

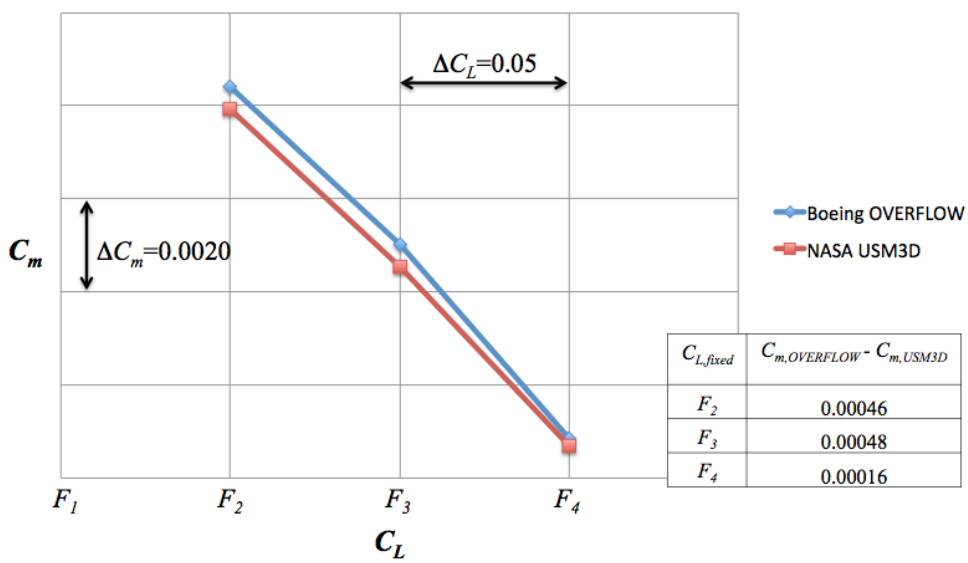

$C_{L,fixed}$	$C_{m,OVERFLOW} - C_{m,USM3D}$
F_2	0.00046
F_3	0.00048
F_4	0.00016

Figure 7. Comparison of C_m between the two codes for the HWB WBT configuration for $M = M_8$ at $C_{L,fixed} = F_2$, F_3, and F_4.

The OVERFLOW analysis used a tighter tolerance to achieve the fixed lift coefficient than was used with USM3D, which resulted in a correspondingly more precise level of C_L when compared with USM3D values of C_L as seen in Figure 5. The USM3D code was improved for a tighter $C_{L,fixed}$ tolerance and the effect was assessed for Mach numbers $M = M_5$, M_6, M_7, M_8, and M_9 for the design lift coefficient F_3. The C_D, C_L, and angle of attack results from USM3D at both tolerance levels are shown in Figure 8 for the HWB WBT configuration over $M_1 \leq M \leq M_{10}$ and at the fixed lift coefficient F_3. The effect of the tighter tolerance in USM3D improved the precision in C_L more closely to that achieved with OVERFLOW, but resulted in very little change in the resultant drag coefficient and angle of attack.

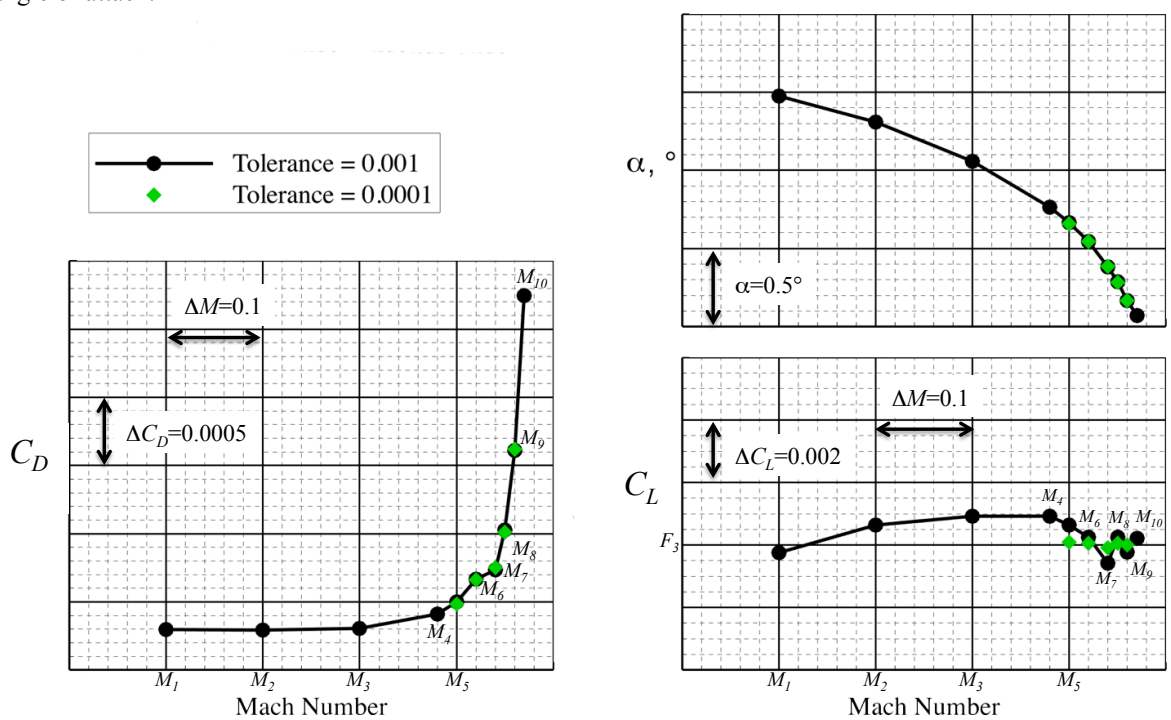

Figure 8. The effect of the tolerance in USM3D for the HWB WBT configuration at selected Mach numbers for $C_{L,fixed} = F_3$.

B. Powered HWB Performance

Initial analyses for the powered HWB configuration will be presented with the center elevon deflection set to zero degrees. Figure 9 shows the USM3D and OVERFLOW drag coefficient predictions for the HWB WBNPT configuration at the cruise Mach number $M = M_8$ with engine power condition of thrust equal to drag (T=D) for the four fixed lift coefficients. The comparison of data between the two results is good; the USM3D results are within 1.6 to 3 drag counts of the OVERFLOW results. Some differences between these complex powered simulations were expected due to turbulence modeling. The OVERFLOW computations used the SA-QCR turbulence model, which improves the accuracy of corner flows compared to corner flows computed with the linear Boussinesq eddy viscosity models (standard SA model of USM3D).

Figure 10 shows the USM3D and OVERFLOW drag coefficient predictions for the HWB WBNPT configuration at the cruise lift coefficient (F_3) with an engine power condition for $T = D$ for three Mach numbers, $M = M_1$, M_5, M_8. The agreement between the codes is better at the cruise design condition of $M = M_8$ and is degraded at the off-design Mach numbers.

The USM3D and OVERFLOW surface pressure coefficient distributions are shown in Figures 11 and 12 for three body stations (*Y1*, *Y2*, and *Y3*) and four wing stations (*Y4*, *Y5*, *Y6*, and *Y7*), respectively. The data are for the powered HWB WBTNP configuration at the design point ($M = M_8$, and $C_{L,fixed} = F_3$). Both the upper and lower surface C_p data are plotted. In general, there is very good agreement in pressure distributions between the two codes for this powered design condition. The predictions are slightly different at midchord of the two outboard wing stations (*Y6* and *Y7*), where OVERFLOW predicts a crisper shock than USM3D, perhaps due to better grid resolution. Additionally, USM3D predicts more suction upstream of the nacelle inlet at body stations *Y1* and *Y2*.

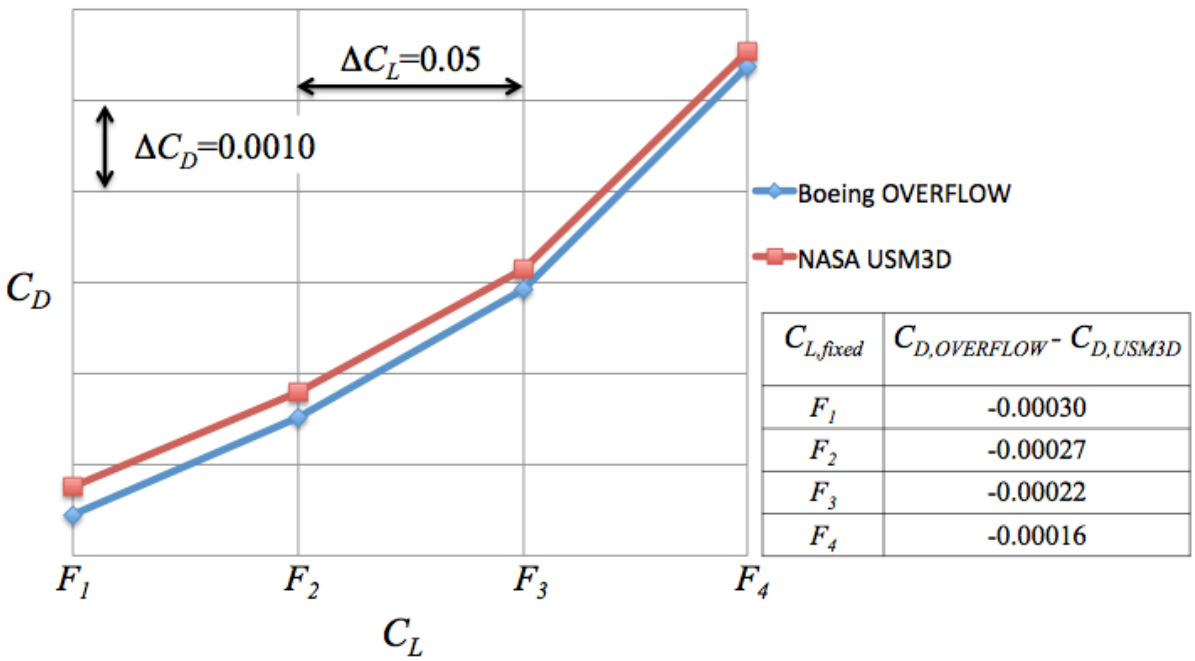

$C_{L,fixed}$	$C_{D,OVERFLOW}$ - $C_{D,USM3D}$
F_1	-0.00030
F_2	-0.00027
F_3	-0.00022
F_4	-0.00016

Figure 9. Comparison of C_D between the two codes for the HWB WBTNP configuration. Center elevon deflection = 0°, $M = M_8$, and an engine power condition of $T=D$.

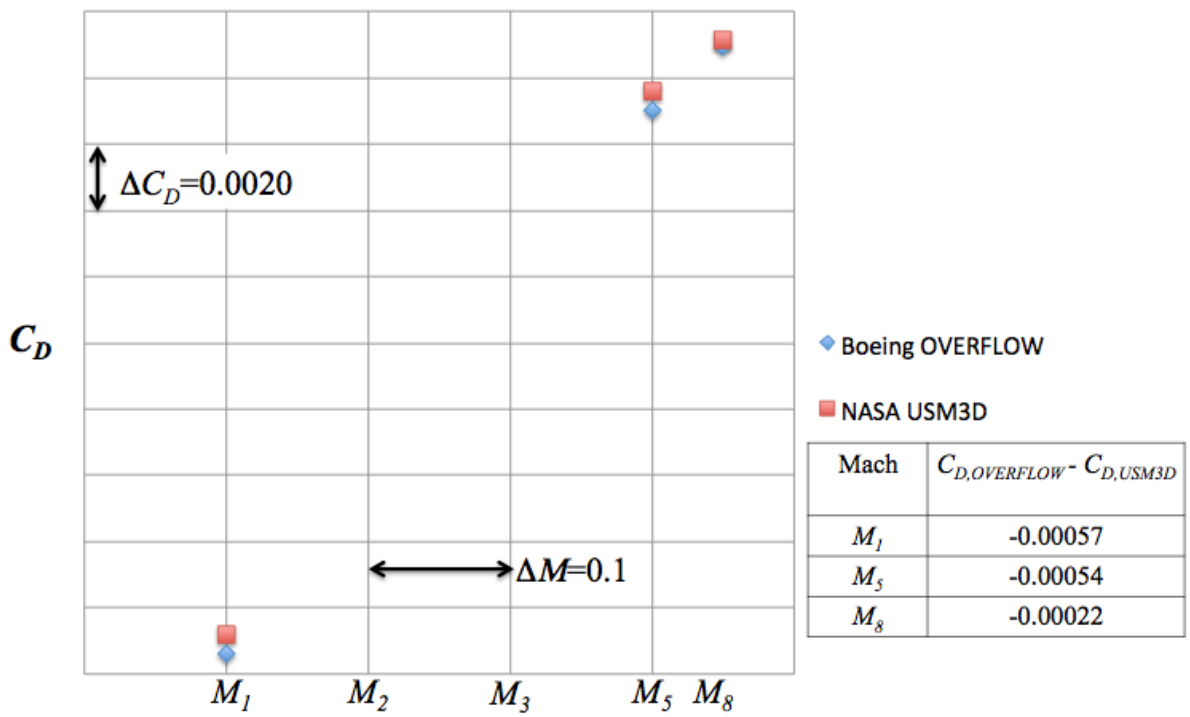

Mach	$C_{D,OVERFLOW}$ - $C_{D,USM3D}$
M_1	-0.00057
M_5	-0.00054
M_8	-0.00022

Figure 10. Comparison of C_D between the two codes for the HWB WBTNP configuration. Center elevon deflection = 0°, $C_{L,fixed} = F_3$, and an engine power condition of $T=D$.

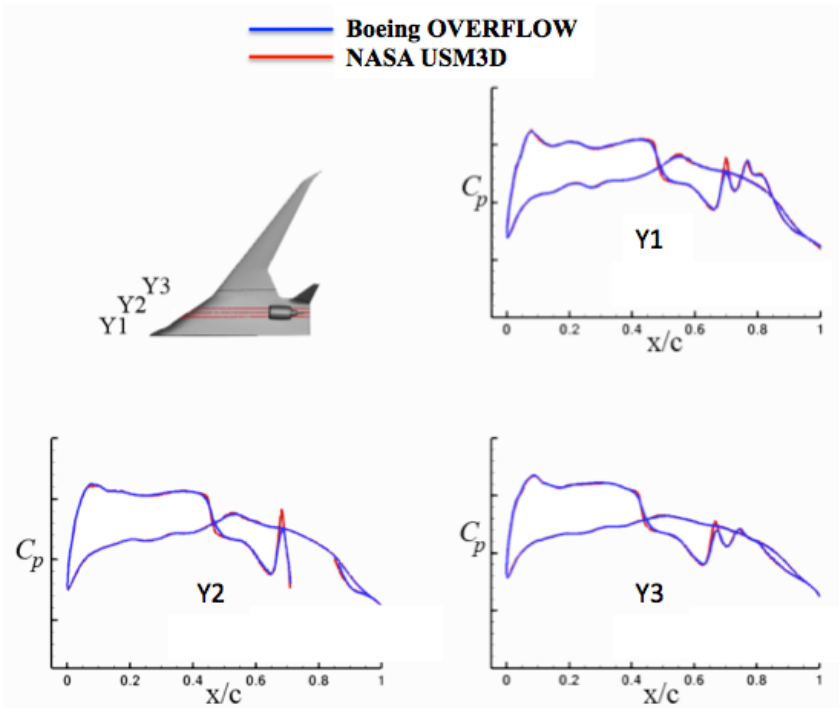

Figure 11. Comparison of C_p between the two codes at 3 stations on the body of the HWB WBTNP configuration. Center elevon deflection = 0°, $M = M_8$, $C_{L,fixed} = F_3$, and an engine power condition of $T=D$.

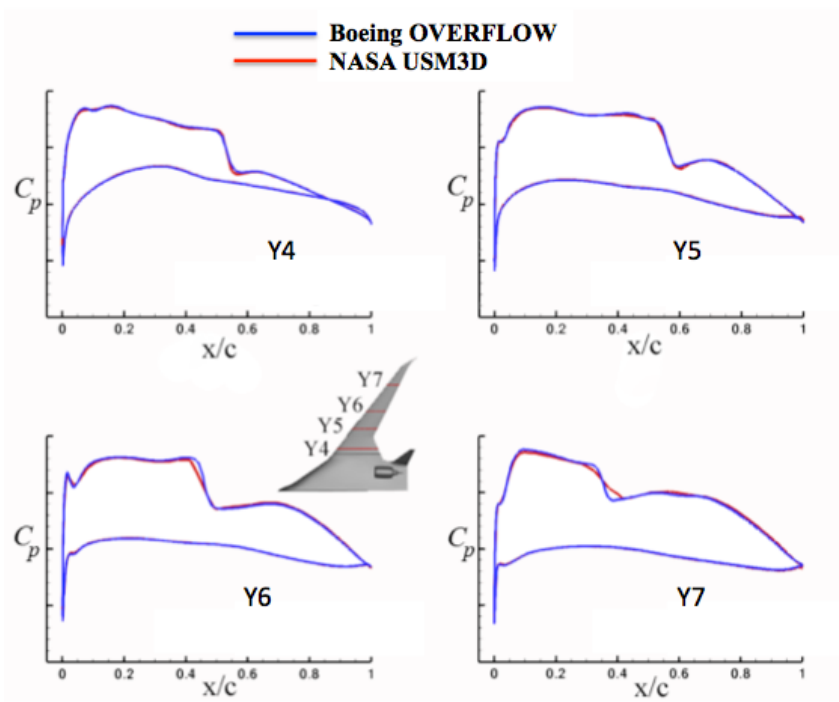

Figure 12. Comparison of C_p between the two codes at 4 stations on the wing of the HWB WBTNP configuration. Center elevon deflection = 0°, $M = M_8$, $C_{L,fixed} = F_3$, and an engine power condition of $T=D$.

Trimmed drag polars are critical to interference drag assessments for a complete aircraft concept, and Boeing incorporated this into their interference drag analysis. Trim was achieved through center elevon deflection, and to assess the elevon effects, NASA performed computations for a limited number of elevon deflection angles. The USM3D and OVERFLOW results for the powered HWB WBTNP configuration with nonzero center elevon deflections are presented next. Figures 13 and 14 show drag coefficient data at the cruise Mach number ($M = M_8$) for the elevon deflection angles of -3° and +3°, respectively. The largest difference in drag occurs at the off-design lift coefficient; with a difference in C_D between the codes of 3.2 counts of drag (Figure 14). A difference between the codes of up to two counts of drag at typical cruise conditions could be associated with the difference in methodology and turbulence models between the codes. The USM3D deflected elevon grids were also found to be coarser than desired around the center elevon. Figures 15 shows the pitching moment coefficient as a function of the center elevon deflection angle for the cruise Mach number ($M = M_8$) and the four fixed lift coefficients. The trend of pitching moment with deflection angle is duplicated well with both codes. The agreement in the magnitude of pitching moment coefficient between the two codes is excellent for the configuration with a center elevon deflected to -3°. The differences in C_m magnitude grows with increase deflection angle but there is still fair agreement between the codes with a center elevon deflected to +3°.

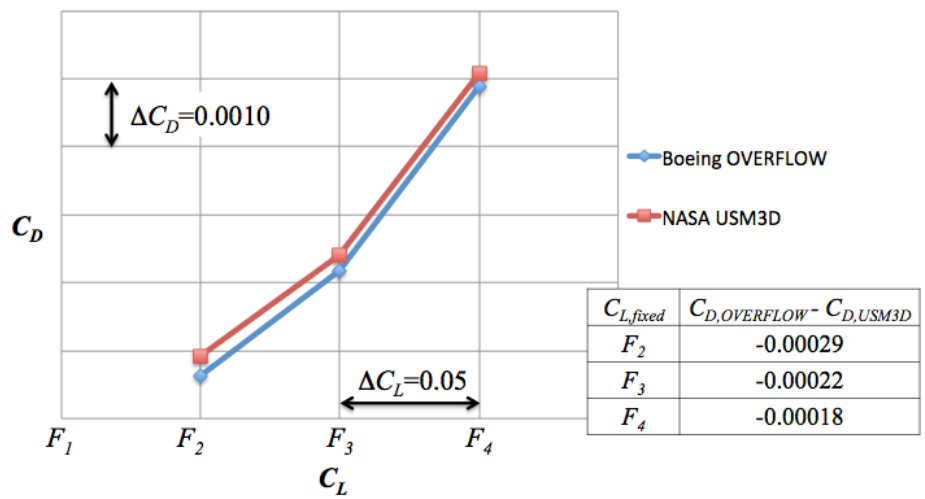

$C_{L,fixed}$	$C_{D,OVERFLOW} - C_{D,USM3D}$
F_2	-0.00029
F_3	-0.00022
F_4	-0.00018

Figure 13. Comparison of C_D between the two codes for the HWB WBTNP configuration. Center elevon deflection = -3°, $M = M_8$, and an engine power condition of $T=D$.

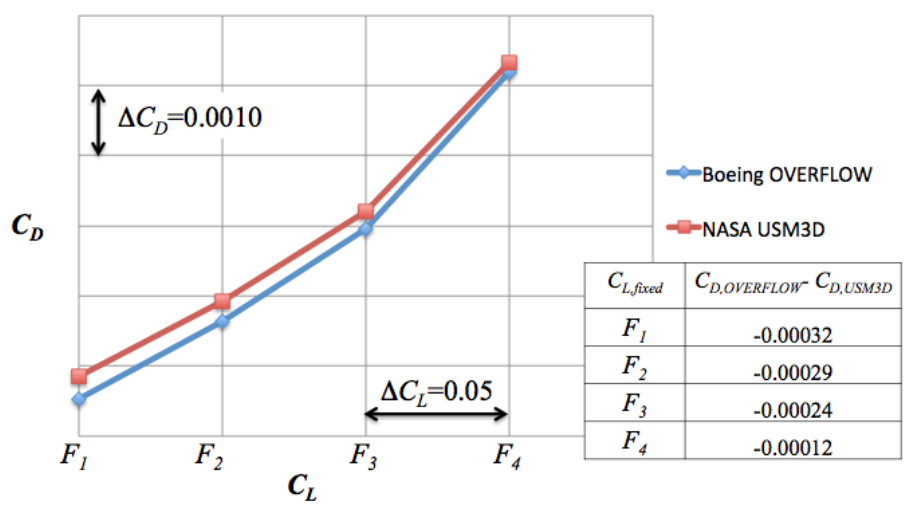

$C_{L,fixed}$	$C_{D,OVERFLOW} - C_{D,USM3D}$
F_1	-0.00032
F_2	-0.00029
F_3	-0.00024
F_4	-0.00012

Figure 14. Comparison of C_D between the two codes for the HWB WBTNP configuration. Center elevon deflection = +3°, $M = M_8$, and an engine power condition of $T=D$.

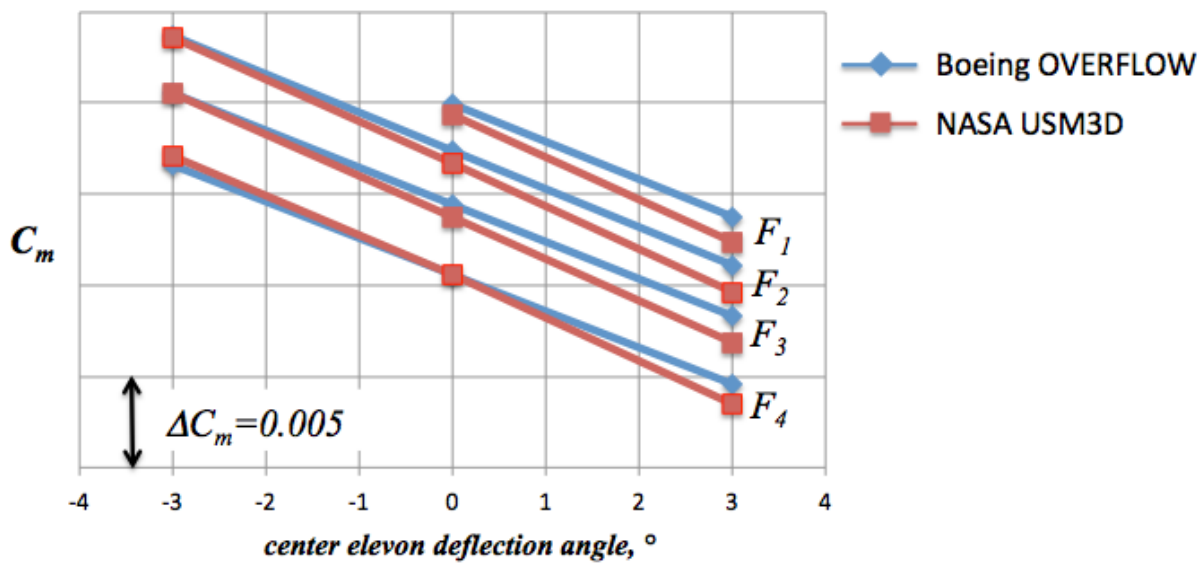

Figure 15. Comparison of C_m between the two codes for the HWB WBTNP configuration for $M = M_8$ and an engine power condition of $T=D$.

Figure 16 shows the USM3D pressure coefficient contours on the upper surface of the HWB WBTNP configuration for the cruise condition ($M = M_8$ and $C_{L,fixed} = F_3$) at center elevon deflection angles of -3°, 0° and +3°. Similar plots for the OVERFLOW solutions are shown in Figure 17. As deflection angle increases from -3° to 0° and then to 3°, the shock moves slightly forward on the body (away from nacelles) and the region of transonic flow on the wing appears to diminish. This is consistent with the reduced angle of attack (as elevon deflection increases) for these fixed lift coefficient results. The increased elevon deflection also induces transonic flow just upstream of the elevon in the vicinity of the aft nacelle pylon. The net effect of these shifts in wing-body loadings, along with the elevon loading itself, is the decreased pitching moment with increasing elevon deflection, at fixed lift coefficient, as shown in Figure 15. As expected from the excellent correlation of pitching moment at a -3° center elevon deflection angle, the flow contours between USM3D and OVERFLOW solution compare very well (Figures 16(a) and 17(a)). The larger difference in C_m between the two codes for a +3° center elevon deflection angle may be associated with the coarser mesh around the elevon for the USM3D solutions. Compared to a compression corner (negative deflection), the coarse mesh had a larger consequence on resolution of the hinge-line expansion from the positive deflection. Detailed comparison of the two solutions for +3° revealed a difference in C_p distribution at the start of the center elevon along the body centerline. Further inspection of the meshes also indicated that the USM3D grid did not resolve the curvature between the body and the deflected center elevon as well as the OVERFLOW grid.

Although trim analysis was not explicitly performed by NASA, the correlation of the center elevon effectiveness between the Boeing/OVERFLOW and the NASA/USM3D CFD results brings confidence to the trim effects facet of an interference drag analysis.

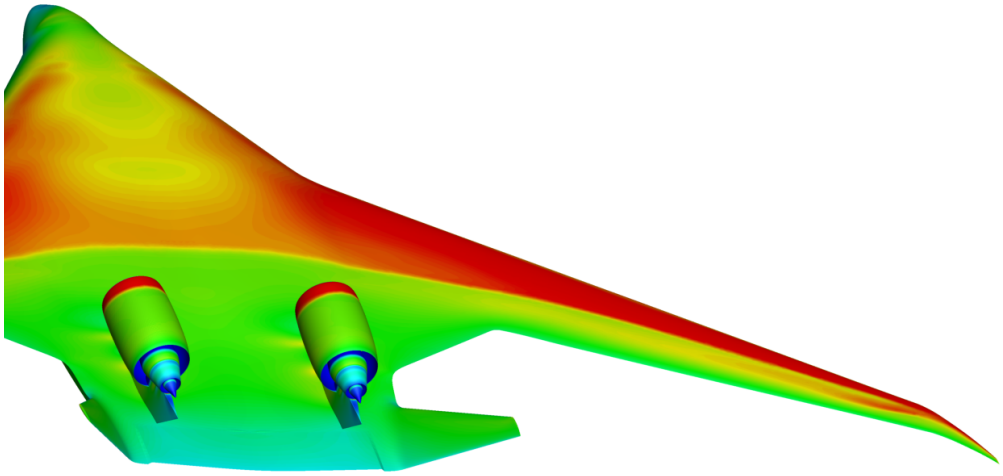

(a) *Center elevon deflected -3°*

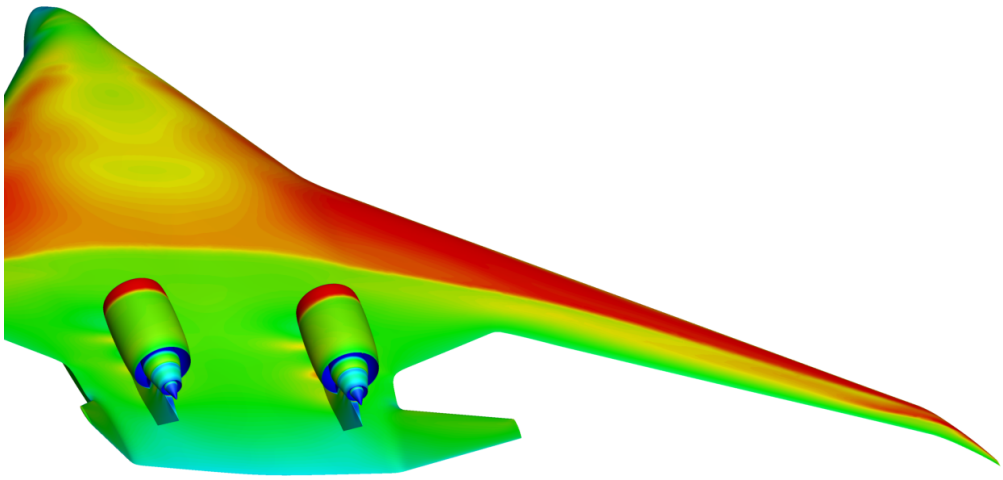

(b) *Center elevon deflected 0°*

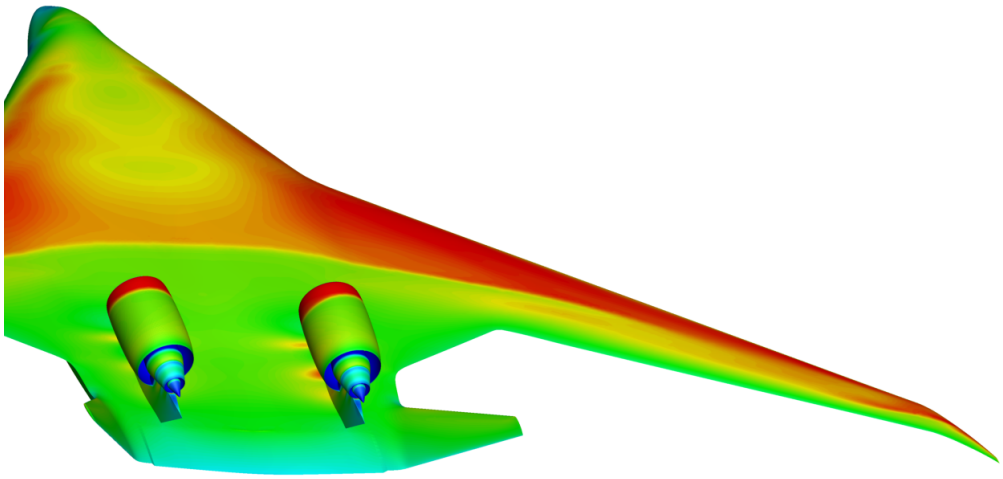

(c) *Center elevon deflected +3°*

Figure 16. Comparison of C_p from USM3D for the HWB WBTNP configuration for $C_{L,fixed} = F_3$, $M = M_8$, and an engine power condition of $T=D$.

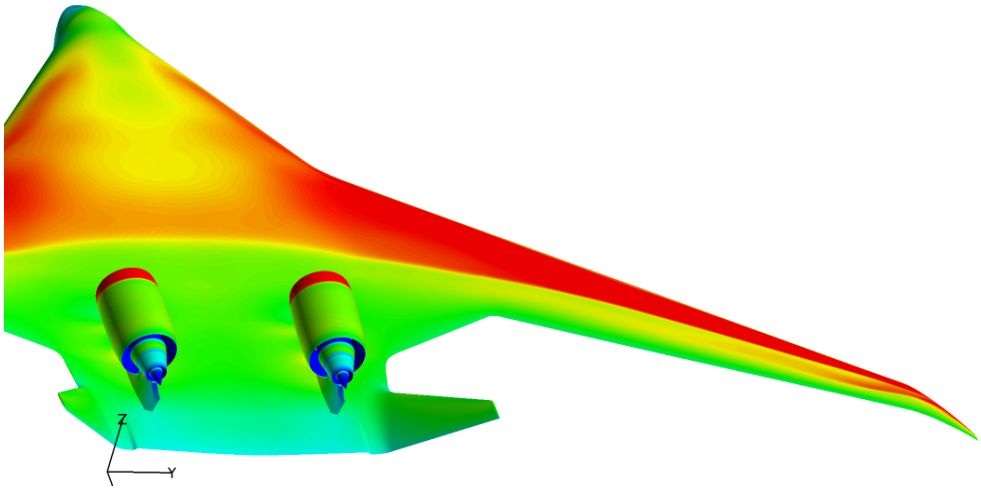

(a) *Center elevon deflected -3°*

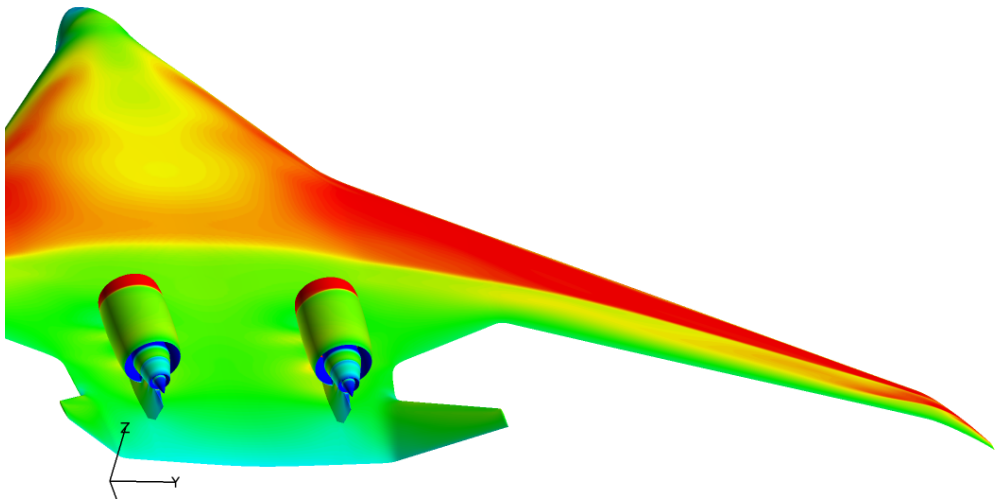

(b) *Center elevon deflected 0°*

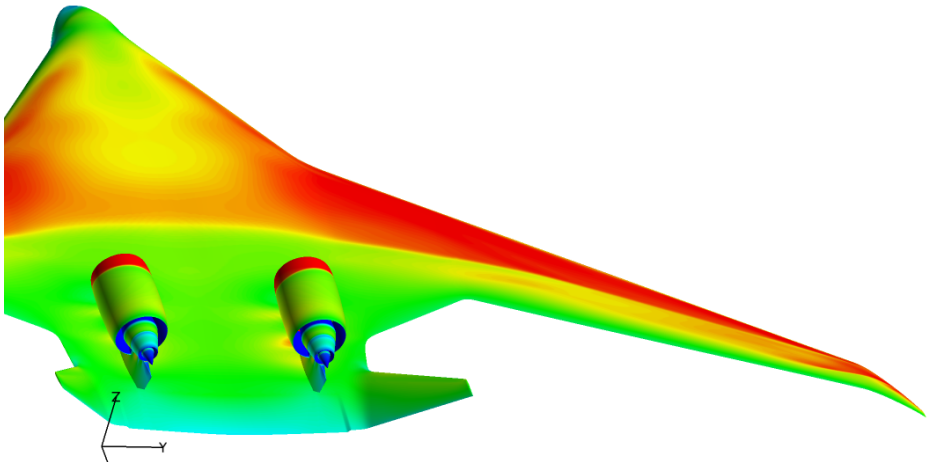

(c) *Center elevon deflected +3°*

Figure 17. Comparison of C_p from OVERFLOW for the HWB WBTNP configuration for $C_{L,fixed} = F_3$, $M = M_8$, and an engine power condition of $T=D$.

C. Isolated Nacelle

The third and final CFD analysis is for the isolated and powered nacelle with the same thrust setting from the full configuration analysis at cruise conditions. Results were computed at the cruise Mach number of $M = M_8$ for the powered nacelle with the same thrust setting used for the complete configuration analysis (i.e., thrust set equal to the complete configuration drag). The thrust setting for results in this paper correspond the the complete configuration drag with the center elevon deflection set equal to zero.

Front and back isometric views of the OVERFLOW and USM3D surface pressure coefficient contours and streamlines on the isolated nacelle are shown in Figures 18 and 19, respectively. Imaging details used for the OVERFLOW and USM3D solution displays were not exactly the same, and qualitative comparison between the two solutions is quite good. Both streamline patterns show extensive regions of attached flow, and they also both indicate a separated vortical region near the lower edge of the splitter plate.

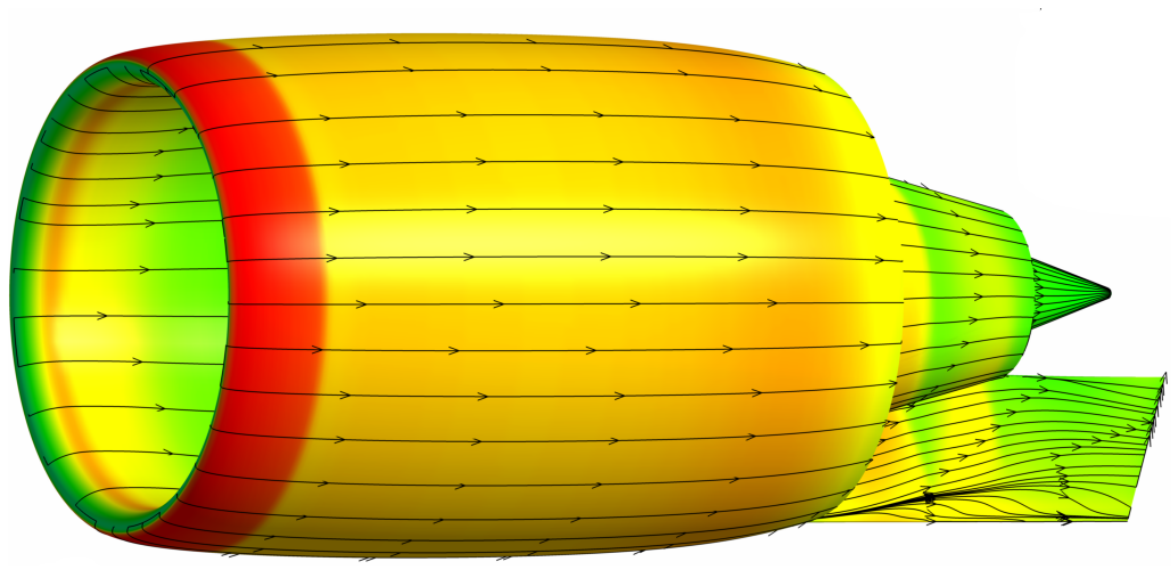

(a) Boeing OVERFLOW

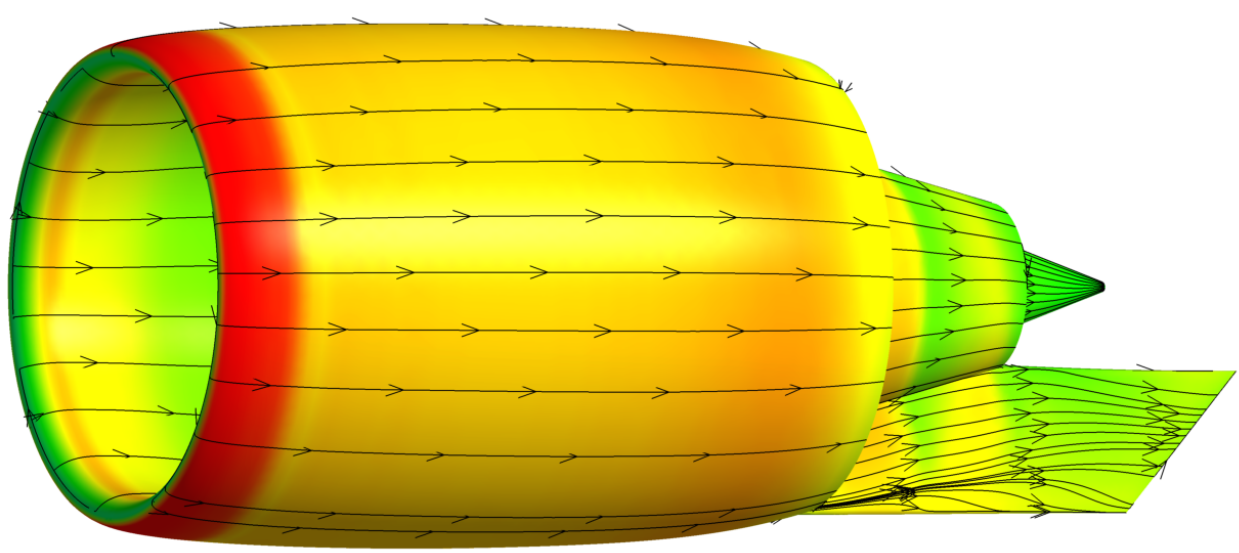

(b) NASA USM3D

Figure 18. A front isometric view of the OVERFLOW and USM3D surface C_p contours and streamlines on the isolated nacelle for $M = M_8$ and an engine power condition of $T=D$.

The good qualitative agreement between the two solutions is evidenced not only for the external portions of the nacelle, but also for the inlet (Figure 18) and the exhaust (Figure 19) internal surfaces. This brings confidence to the propulsion boundary conditions used in the two codes.

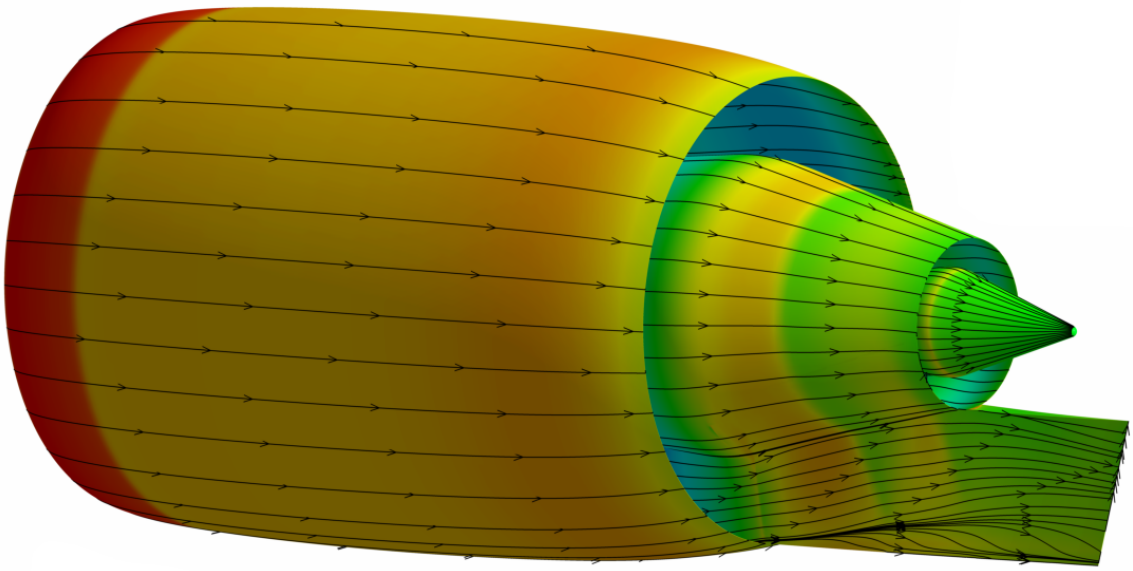

(a) Boeing OVERFLOW

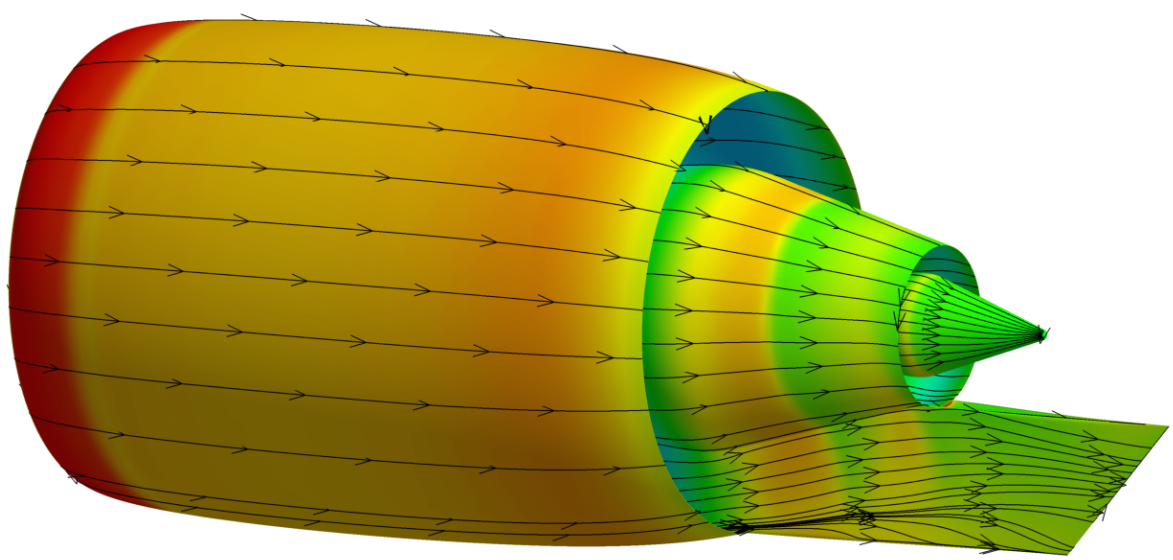

(b) NASA USM3D

Figure 19. A back isometric view of the OVERFLOW and USM3D surface C_p contours and streamlines on the isolated nacelle for $M = M_8$ and an engine power condition of $T=D$.

The USM3D and OVERFLOW pressure coefficient distributions on the top and the side of the isolated nacelle are shown in Figures 20 and 21, respectively. The computed results for the same conditions discussed with Figures 18 and 19 ($M = M_8$., $T = D$). There is excellent agreement between the codes along the top of the nacelle (Figure 20) and along the side of the nacelle (Figure 21). Additionally, the difference in drag coefficient for the two methods is 0.0002237, or 2.237 drag counts. Some difference is expected from the slight difference in the geometry at the bifurcator trailing edge used by the two CFD methods. The geometry used for USM3D solution has more wetted area and therefore the slightly higher drag is expected. Good agreement between the two codes for the powered CFD of the isolated nacelle is important to bring confidence to drag buildup and interference analyses.

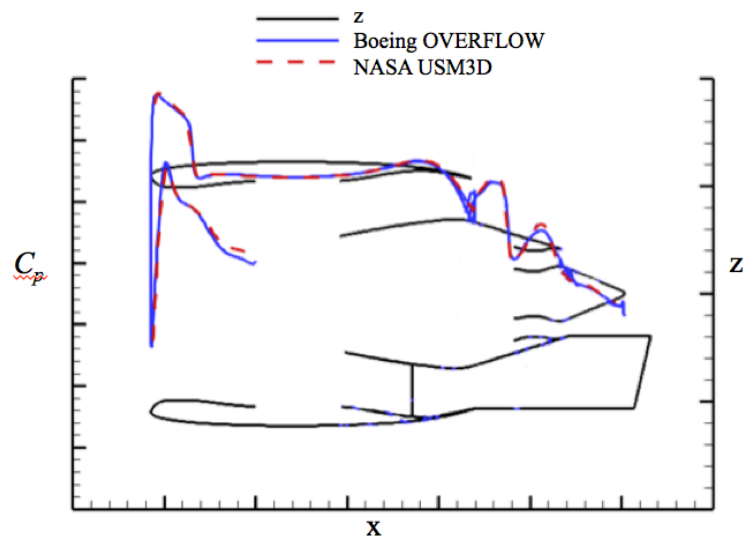

Figure 20. Comparison of C_p between the two codes along the top of the isolated nacelle for $M = M_8$ and an engine power condition of $T=D$.

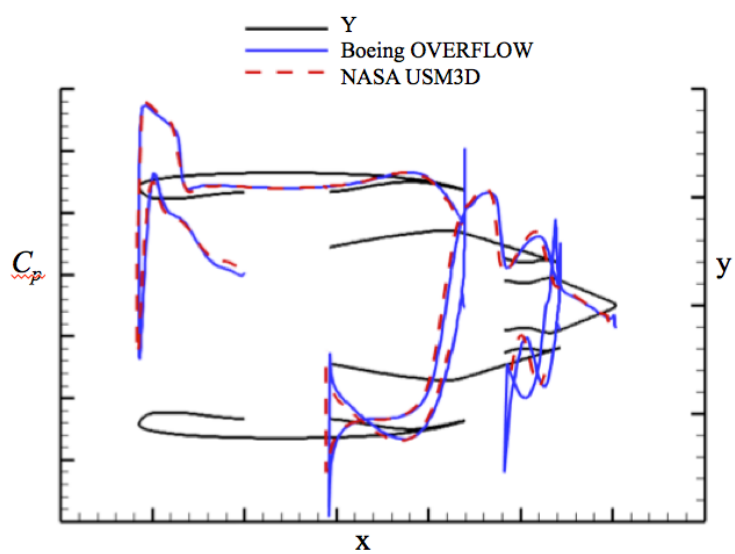

Figure 21. Comparison of C_p between the two codes along the side of the isolated nacelle for $M = M_8$ and an engine power condition of $T=D$.

VII. Conclusion

NASA and Boeing created a partnership in the ERA project to evaluate a Hybrid Wing-Body aircraft concept that minimizes adverse propulsion/airframe integration effects and meets ERA noise reduction metrics. The team used computational fluid dynamics predictions and a series of wind tunnel tests to quantify key design trade-space issues that impact UHB engine operability in HWB concepts and to minimize the impact of adverse effects on the aerodynamic metrics. Although new low-speed testing was conducted under ERA, the ERA project was forced to eliminate the transonic wind tunnel test due to resource restrictions. Hence, two independent CFD-based analyses were performed to bring confidence to a numerically determined interference drag increment. The focus of the study was on comparisons from the two CFD studies for three configurations that form critical input to the interference drag analysis process. All work was performed at full-scale conditions.

The primary analysis was performed by Boeing to define the HWB performance, and a proprietary version of the structured-mesh flow solver OVERFLOW that includes a thrust-drag accounting system was used. The secondary analysis was performed by NASA LaRC to add confidence to the OVERFLOW results, and the unstructured mesh flow solver USM3D was used.

Comparisons between the CFD results were presented for a powered complete configuration, the configuration with the nacelle/pylon removed, and for the isolated and powered nacelle. Very good correlations were shown not only for forces and moments but also for surface pressure coefficients despite some minor geometric differences in the two analyses. Some differences between the CFD results were also expected due to a more physically representative turbulence model used with OVERFLOW that was not available in USM3D. Nonetheless, many correlations for drag coefficient were within 1 to 3 counts up to cruise conditions and through drag rise. The largest drag difference was about 6 counts for the powered complete configuration at an off-design Mach number. The good agreement between the two independent CFD analyses adds confidence to the numerical aerodynamic performance predictions and the associated calculation of interference drag.

Acknowledgments

The authors would like to thank Ed Parlette for his excellent gridding contributions and providing quality grids for the USM3D numerical simulations. His work in the ERA project was highly valued.

References

[1]Bonet, John T.; Schellenger, Harvey G.; Rawdon, Blane K.; Elmer, Kevin R.; Wakayama, Sean R.; Grown, Derrell L.; and Yueping Guo: "Environmentally Responsible Aviation (ERA) Project – N+2 Advanced Vehicle Concepts Study and Conceptual design of Subscale Test Vehicle (STV)," NASA/CR-2011-216519, December 2011.

[2]Nichols, R. H. and Buning, P. G., User's Manual for OVERFLOW Version 2.2, University of Alabama and NASA Langley Research Center, August 2010.

[3]Gatzke, T. D., LaBozzetta, W. F., Finfrock, G. P., Johnson, J. A., and Romer, W. W., MACGS: A Zonal Grid Generation System for Complex Aero-Propulsion Configurations, AIAA Paper 91-2156, June 1991.

[4]Chan, W. M., Chiu, I. T., and Buning, P. G., User's Manual for the HYPGEN Hyperbolic Grid Generator and the HGUI Graphical User Interface, NASA-TM 108791, October 1993.

[5]Chan, W. M., Rogers, S. E., Pandya, S. A., Kao, D. L., Buning, P. G., Meakin, R. L., Boger, D. A., and Nash, S. M., Chimera Grid Tools User's Manual, Version 2.1, NASA Ames Research Center, March 2010, http://people.nas.nasa.gov/wchan/cgt/doc/man.html.

[6]Shus, N. E., Dietz, W. E., Nash, S. M., Baker, M. D., and Rogers, S. E., PEGASUS User's Manual Version 5.1c, MICROCRAFT, July 2000.

[7]Vassberg, J. C., DeHaan, M. A., and Sclafani, A. J., "Grid Generation Requirements for Accurate Drag Prediction Based on OVERFLOW Calculations," AIAA Paper 2003-4124, 16th AIAA Computational Fluid Dynamics Conference, Orlando, FL, June 2003.

[8]Chan, W. M. and Buning, P. G., User's Manual for FOMOCO Utilities Force and Moment Computation Tools for Overset Grids, NASA-TM 110408, July 1996.

[9]Frink, N. T., Pirzadeh, S. Z., Parikh, P. C., Pandya, M. J., and Bhat, M. K., "The NASA Tetrahedral Unstructured Software System," The Aeronautical Journal, Vol. 104, No. 1040, pp. 491–499, October 2000.

[10]Pao, S. P., "USMC6-TetrUSS Grid and Solution Cutter: A Brief Users' Guide," Version 4, NASA Langley Research Center, October 2008.

[11]Samareh, J., "GridTool: A Surface Modeling and Grid Generation Tool," Proceedings of the Workshop on Surface Modeling, Grid Generation, and Related Issues in CFD Solutions, NASA CP–3291, May 9–11, 1995.

[12]Pirzadeh, S., "Unstructured Viscous Grid Generation by Advancing-Layers Method," AIAA Journal, Vol. 32, No. 8, pp. 1735–1737, August 1994.

[13]Pirzadeh, S., "Structured Background Grids for Generation of Unstructured Grids by Advancing Front Method," AIAA Journal, Vol. 31, No. 2, pp. 257–265, February 1993.

[14]Pandya, M. J., Abdol-Hamid, K. S., and Frink, N. T., "Enhancement of USM3D Unstructured Flow Solver for High-Speed High-Temperature Shear Flows," AIAA 2009-1329, The 47th AIAA Aerospace Sciences Meeting, January 5-8, 2009.